

The wings of Ca II H and K as solar fluxtube diagnostics

V. A. Sheminova¹, R. J. Rutten^{2,3}, and L. H. M. Rouppe van der Voort^{3,4}

¹ Main Astronomical Observatory, National Academy of Sciences of the Ukraine, 27 Akademika Zabolotnoho St., 03680 Kiev, Ukraine

e-mail: shem@mao.kiev.ua

² Sterrekundig Instituut, Utrecht University, Postbus 80 000, 3508 TA Utrecht, The Netherlands

³ Institute of Theoretical Astrophysics, University of Oslo, PO Box 1029 Blindern, 0315 Oslo, Norway

⁴ Center of Mathematics for Applications, University of Oslo, PO Box 1053 Blindern, 0316 Oslo, Norway

Received 22 December 2004 / Accepted 15 March 2005

Abstract. We combine high-resolution Ca II H and K spectrograms from the Swedish Vacuum Solar Telescope with standard fluxtube modeling to derive photospheric temperature and velocity stratifications within individual magnetic elements in plage near a sunspot. We find that 1D on-axis modeling gives better consistency than spatial averaging over flaring-fluxtube geometry. Our best-fit temperature stratifications suggest that magnetic elements are close to radiative equilibrium throughout their photospheres. Their brightness excess throughout the H and K wings compared with the quiet photosphere is primarily due to low density, not to mechanical heating. We conclude that the extended H and K wings provide excellent fine-structure diagnostics for both high-resolution observations and simulations of the solar photosphere.

Key words. Sun: photosphere – Sun: magnetic fields – Sun: faculae, plages

1. Introduction

The extended wings of the Ca II H and K lines in the solar spectrum provide straightforward and informative diagnostics of the temperature and line-of-sight velocity stratifications of the solar photosphere. In this paper we use H and K wing spectrometry to derive such stratifications within individual magnetic elements of the type which grouped together constitute active-region plage. We so follow the classical example of solar plage modeling by Shine & Linsky (1974), but we exploit the subsequent improvement in angular resolution to diagnose individual magnetic elements rather than spatially unresolved plage. Since the advent of high-order adaptive optics at new solar telescopes promises substantial further advance, in particular at the Swedish 1-m Solar Telescope (SST), our analysis represents a pilot study for Ca II H and K wing spectrometry at yet higher resolution.

Plage and network on the solar surface consist largely of discrete strong-field magnetic elements (Livingston & Harvey 1969; Howard & Stenflo 1972; Frazier & Stenflo 1972) that have been modeled as magnetostatic fluxtubes since the pioneering work of Spruit (1976, 1977). Observationally they are known as magnetic knots (Beckers & Schröter 1968), filigree (Dunn & Zirker 1973), network bright points (Muller 1983), and G-band bright points (Muller & Roudier 1984). They appear bright through the hot-wall radiation which escapes through the tenuous tube interior (Spruit 1976; Spruit & Zwaan 1981), as confirmed by the recent MHD simulations of Keller et al. (2004) and Carlsson et al. (2004). These new

3D simulations crown two decades of magnetic-element modeling, in particular empirical fluxtube modeling at Zürich (e.g. Solanki 1986; Keller et al. 1990; Solanki et al. 1991; Solanki & Brigljevic 1992; Bünte et al. 1993; Bruls & Solanki 1993) and numerical fluxsheet simulation at Freiburg (e.g. Knölker & Schüssler 1988; Grossmann-Doerth et al. 1994, 1998; Steiner 1998, 2005). The principal aims of these and comparable studies are to elucidate the nature of magnetic elements and how they form, evolve and interact within the wider context of understanding the structure, dynamics, and energy balance of the outer solar atmosphere to which they represent magnetic “footpoints” constraining the field topology and energy budget.

In this paper we interpret high-resolution Ca II H and K spectra of individual magnetic elements located within plage near a sunspot. We apply classical magnetostatic thin-fluxtube modeling (e.g. Solanki & Steiner 1990) but without spatial averaging over upward-expanding and canopy-merging magnetostatic fluxtubes as in the “inverted wine-glass” Zürich approach of Bünte et al. (1993). We instead employ 1D columnar modeling to derive stratifications along tube axes as if our spectra result from fully resolved vertical fluxtubes. This is obviously optimistic, but such resolved-pixel spectrometry is bound to become increasingly realistic and to become the basis for large-volume data inversions.

2. Observations

We use the best spectrograms in the observations described in Rouppe van der Voort (2002a). They were obtained with

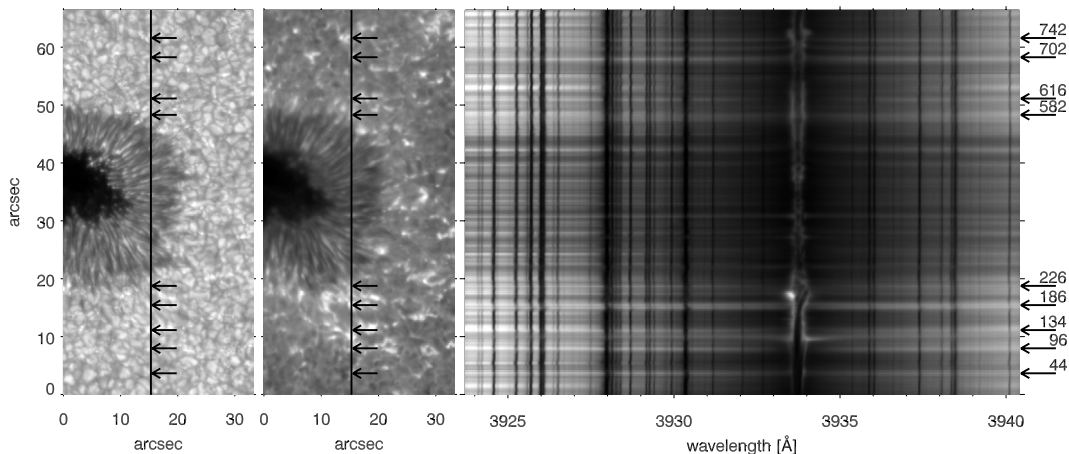


Fig. 1. Ca II K spectrometry of active region AR8704. The two strip images are segments of G-band and Ca II K filtergrams, respectively. The superimposed vertical line defines the slit location. The corresponding Ca II K spectrogram is shown at right. Line center is at 3933.7 Å. The arrows specify the nine analyzed locations along the slit, identified by their pixel row numbers at right.

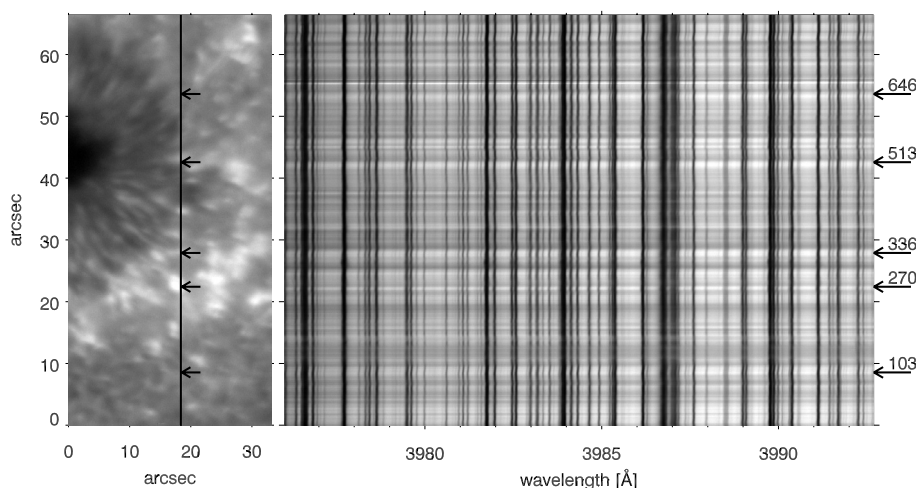


Fig. 2. Ca II H data in the same format as Fig. 1 but without G-band image. The spectral segment lies in the outer red wing of Ca II H (line center at 3968.5 Å), close to the opacity minimum near 4000 Å. The arrows identify the five selected bright points. The angular resolution is less good than in Fig. 1.

the former Swedish Vacuum Solar Telescope (SVST; Scharmer et al. 1985) on La Palma and consist of simultaneous spectrograms and filtergrams of the leading sunspot of active region NOAA 8704 taken on September 22, 1999 using correlation tracking and frame selection. The spot was located at 20.0° S, 4.0° E, $\mu = 0.88$. A Dutch Open Telescope movie of this spot a day later can be downloaded as the February 23, 2000 entry from the “Astronomy Picture of the Day”.

The SVST observations concentrated on the spot; the extensive analysis reported in Rouppe van der Voort (2002a) concentrated on its penumbra. However, the field of view also contained plage and relatively quiet areas besides the spot. In this paper we use the very best Ca II K spectrogram, taken during a moment of exceptional seeing quality, to analyze spatially resolved Ca II K spectra from nine selected bright points in the spot surroundings. In addition, we model five Ca II H bright points in the best but less good spectrogram obtained later on the same day after resetting the spectrograph to the outer red wing of Ca II H. Both spectrograms are 350 ms exposures with the SVST’s Littrow spectrometer (Scharmer et al. 1985). The slit width of 25 μm corresponded to 0.23 arcsec angular and 30 mÅ spectral resolution, the 9 μm CCD pixel size to

11 mÅ spectral and 0.083 arcsec spatial sampling. The solar scene was simultaneously imaged using slit-jaw reflection with a 12 Å G-band filter centered on $\lambda = 4305$ Å and a 3 Å filter centered on Ca II K (3933.7 Å). The data reduction included dark-frame subtraction, flat-field division, correction for stray-light, and noise filtering as detailed in Rouppe van der Voort (2002a, b).

Figures 1 and 2 display our data. The strip images are cutouts from the G-band and Ca II K slit-jaw filtergrams. The location of the spectrometer slit is indicated with superimposed vertical lines. The arrows identify the selected nine Ca II K bright points and five Ca II H bright points.

The spectrogram in Fig. 1 is one of the best ever taken with the SVST and nearly reaches the 0.2 arcsec SVST diffraction limit at Ca II K. We selected the nine marked locations along the slit for analysis by their bright-point appearance in the images and their fairly symmetrical bright-wing appearance in the spectrum. These bright wing streaks may not be fully resolved but they are relatively well-defined in this high-quality spectrogram. Notice the conspicuous line gaps (Sheeley 1967) with attendant redshift in the far-wing blends, e.g. for the bright point at 186.

The very bright K_{2V} feature between locations 186 and 226 is accompanied by large K_3 redshift. Its marked asymmetry, most likely caused by large chromospheric downflow, and its lack of bright moustache extensions give it closer resemblance to acoustic-shock internetwork K_{2V} grains than to Ellerman bombs (cf. Rutten & Uitenbroek 1991; Carlsson & Stein 1997). The bright points selected here have smaller K_2 asymmetry, but still show considerable variation in their double-peaked K-line cores (Fig. 5). The latter are not addressed here but may be modeled with chromospheric temperature rises within magnetic elements as in the H and K study of Solanki et al. (1991) and the similar analyses of other strong lines by Bruls & Solanki (1993) and Briand & Solanki (1995).

The five slit locations marked in Fig. 2 were selected by their spectral appearance alone, because there was no corresponding G-band image while the slit position on the Ca II K image is less certain due to focus chromaticity.

3. Methods

The Ca II H and K wings as diagnostics. The H and K wings provide excellent diagnostics of photospheric temperature and velocity stratifications. They span a relatively large height range, reaching from the very deepest observable layers (the continuous opacity minimum at 4000 Å which produces effectively as deep sampling as the minimum at 1.6 μm, see Ayres 1989) up to layers about 350 km above the $\tau_5 = 1$ surface (optical depth unity in the continuum at 5000 Å) along the extent of the wing parts for which LTE (Local Thermodynamic Equilibrium) is a good approximation for the Ca II H and K source functions. Within about 1 Å from line center coherent scattering becomes important (e.g. Shine et al. 1975; Ayres 1975; Uitenbroek 1989). LTE is also a good assumption for the line opacity because calcium is predominantly singly ionized throughout the photosphere so that the H and K opacity has small sensitivity to the ultraviolet overionization which complicates the formation of, e.g. Fe I lines (Rutten & Kostik 1982) and alkali lines (Bruls et al. 1992). These two LTE properties together make the Ca II H and K wings relatively easy diagnostics.

In addition, the H and K wings contain both suitable blend-free wing windows and suitable blends to sample this height range with relatively fine meshes both in brightness temperature and in Dopplershift.

Modeling approach. For each bright point selected in Figs. 1 and 2 we have derived empirical best-fit models through trial-and-error adjustment of the temperature stratification in a one-dimensional magnetostatic thin-fluxtube model until the computed H and K wings match the observed ones.

In principle, this technique is similar to the classical line-wing modeling by, e.g. Shine & Linsky (1974) of solar plage and by Ayres et al. (1974), Ayres & Linsky (1975), and Ayres (1975, 1977) of the solar photosphere and other cool-star photospheres. It was applied more recently to sunspot penumbrae (including other spectrograms of the data set used here) by Rouppe van der Voort (2002a).

Here, we apply H and K wing modeling to individual magnetic elements as represented by classical model fluxtubes. We use the thin-tube approximation, (e.g. Defouw 1976; Roberts & Webb 1978; Priest & Forbes 2001) following the standard recipe described in, e.g. Solanki & Steiner (1990) and Sect. 2 of Bellot Rubio et al. (1996), but without data inversion and without spatial integration over flaring and merging fluxtube geometry as in Zürich wine-glass averaging (e.g. Bunte et al. 1993). We instead use one-dimensional on-axis modeling and so effectively assume magnetic filling of order unity, i.e. that our spectra sample magnetic elements as being horizontally homogeneous within the resolution element. It is unlikely that they actually are, but the quality of our spectra warrants this approach and we found that it gives better consistency than spatial wine-glass averaging, as discussed below.

Spectral synthesis and model construction. We use the SPANSAT code described by Gadun & Sheminova (1988) for LTE spectral synthesis of the full overlapping H and K lines including superimposed blends. It computes optical intensity spectra containing any selection of overlapping spectral lines from a given one-dimensional model atmosphere. Our blend list for the spectral region shown in Fig. 3 contains 2914 lines of which the parameters were taken from the VALD database (Kupka et al. 1999; URL <http://www.astro.univie.ac.at/~vald>).

In our trial-and-error fitting we combined the SPANSAT code for each new tube-interior temperature stratification with re-computation of the gas and electron pressures assuming vertical hydrostatic equilibrium and including LTE evaluation of the ionization equilibria for all pertinent elements. The procedure also includes thin-tube horizontal magnetostatic evaluation of the magnetic field stratification. It follows Eqs. (1)–(3) of Bellot Rubio et al. (1996), which fully define isolated thin magnetostatic fluxtubes by the inside and outside temperature stratifications plus the values of the tube radius, field strength, and outside gas pressure at the tube base. The outside model (HSRA-SP-M) and the standard fluxtube model (PLA) from which we take these base values are discussed in the next section.

A major problem that formerly affected such line-wing synthesis concerned the amount of collisional damping by neutral hydrogen atoms. It was commonly fudged through the application of an arbitrary “damping enhancement factor”, but this uncertainty has largely vanished with the quantum-mechanical estimation method of Barklem & O’Mara (1998) which we apply here.

Another classic fudge problem is posed by the “line haze” consisting of the multitude of weak lines in this part of the spectrum (Labs & Neckel 1972). This problem is now largely remedied through the advent of large spectral line databases as VALD. We mimic the remainder in classical fashion by applying scaling factors f to the computed continuous opacity with height dependence $f = 1 + c(N_H/N_{H^-})$, assuming that the missing line-haze opacity scales with the total hydrogen density whereas the computed opacity is dominated by H^- ionization. We determined f values across the H and K region for various

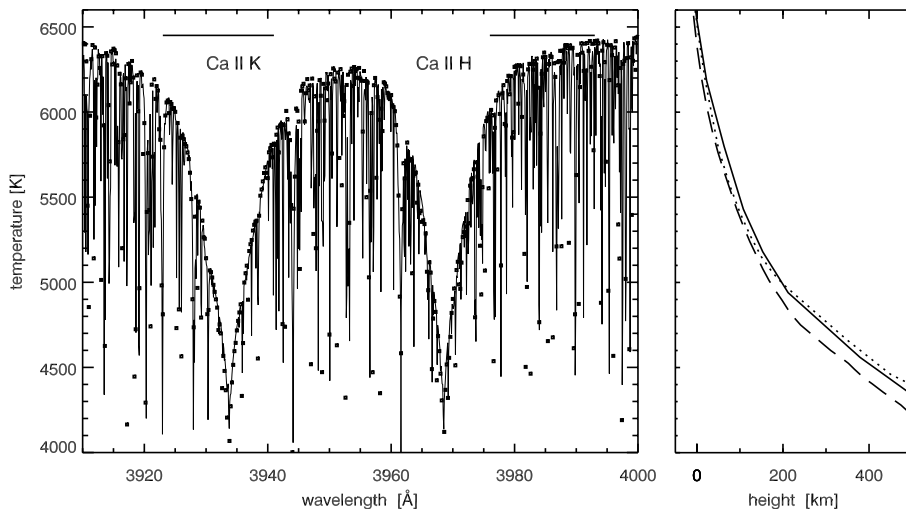


Fig. 3. Adaptation of the HSRA-SP standard model. *Left:* solar disk-center intensity spectrum in the Brault-Neckel atlas converted to brightness temperature. The squares result from spectrum synthesis at 0.2 \AA sampling using HSRA-SP-M which was constructed by fitting the H and K wing windows between blends. The horizontal bars above the spectrum mark the segments covered by the spectrograms in Figs. 1 and 2. They are enlarged in Fig. 4. *Right:* HSRA-SP-M temperature stratification (solid) compared with the HSRA-SP (dashed) and FALC (dotted) models. The height scale has its zero point at $\tau_5 = 1$ for each model.

standard solar photosphere models by fitting synthetic outer H and K wings to the observed ones in the Brault-Neckel atlas. The latter tabulates high-quality disk-center spectra taken by Brault with the NSO Fourier Transform Spectrometer (Brault 1978, 1993) which were made available by Neckel (1999) after calibration to the absolute intensities of Neckel & Labs (1984). These best-fit opacity enhancements differ considerably between different models, as specified below. We suspect that the larger values correct primarily for deficiencies of the 1D model stratifications, especially in deep layers, and we therefore used the smallest standard-model values in our bright-point fitting. Their effect is nearly negligible, so that we effectively assume that the VALD blend list is sufficiently complete.

Reference quiet-sun model. As outside quiet-sun model we use a doubly modified version of the HSRA of Gingerich et al. (1971). It was extended as HSRA-SP into deeper layers by Spruit (1974) taking convective energy transport into account. Due to the latter inclusion, this model remains the 1D model of choice to describe the deepest layers of the spatially-averaged non-magnetic photosphere. Our own modification, called HSRA-SP-M henceforth, is an adjustment of the middle and upper photosphere based on a Ca II H and K fit to the Brault-Neckel atlas. Such adjustment is necessary because already the analysis of Ayres (1977) made clear that the HSRA has too low upper-photosphere temperatures to reproduce the inner Ca II H and K wings, whereas the hotter HOLMUL model of Holweger & Müller (1974) did quite well. The difference between these empirical models was attributed by Rutten & Kostik (1982) to NLTE-masking in HOLMUL through its LTE assumption for the iron excitation and ionization equilibria. However, the subsequent modification of the HSRA-like VALC model of Vernazza et al. (1981) to the FALC model of Fontenla et al. (1993), which included better line-blanketing estimation in NLTE iron ionization (Avrett 1985), brought also the upper-photosphere temperature of this empirical NLTE model closer to HOLMUL – but with awkward ad-hoc assumptions regarding line-haze scattering (see Rutten 2002, for a review). Presently, the tide turns again since the more recent update of the HOLMUL by

Grevesse & Sauval (1999) brings LTE iron-line fitting back to the HSRA and therefore into conflict with FALC (although the authors did not notice), while also Bellot Rubio & Borrero (2002) prefer such a cool model as representing a better spatial average over granulation.

We exploit the LTE character of the Ca II H and K wings to provide an independent gauge of this upper-photosphere issue. The outer wings yielded estimates of line-haze scaling factors f by fitting the Brault-Neckel atlas with each model. They are, with slight variation across the H and K wings, $f \approx 1.14$ for HOLMUL, $f \approx 1.05$ for VALC, and $f \approx 1.01$ for HSRA-SP, where these values apply to zero height defined by $\tau_5 = 1$. We adopted the smallest value in our profile fitting on the suspicion that the larger f values represent deep-layer model deficiencies, and then obtained a temperature stratification matching the disk-center spectrum in the Brault-Neckel atlas from the inner H and K wings. The lefthand panel of Fig. 3 shows the resulting best-fit synthesis. The intensities are converted to brightness temperature through Planck function inversion in order to display the temperature regime sampled by the wings. The corresponding HSRA-SP-M model in the righthand panel of Fig. 3 is 100–150 K hotter than the HSRA (or HSRA-SP) in the upper photosphere and matches FALC closely, in conflict with Grevesse & Sauval (1999). This upper-photosphere modeling issue remains undecided in the absence of proper 3D NLTE radiation-hydrodynamics vindication of the LTE assumptions (for both source function and opacity) for iron-line cores (of both Fe I and Fe II) made in HOLMUL-like modeling and of the line-haze scattering assumptions made in FALC-like modeling. We therefore use our more rightfully LTE-based HSRA-SP-M as outside model.

Reference fluxtube model. We use the standard fluxtube model PLA for solar plage constructed by Solanki & Brigglijevic (1992) and shown, e.g. in Fig. 1 of Bruls & Solanki (1993) as the initial model defining our fluxtube base input parameters. They are, respectively, fluxtube diameter 200 km, field strength 2450 Gauss, and outside gas pressure $5 \times 10^5 \text{ dyne cm}^{-2}$ at height $h = -306 \text{ km}$.

We also plot results from the PLA model itself in some of our figures for comparison. These are obtained through two-dimensional spectrum synthesis using fluxtube geometry and ray definition codes kindly provided by S. K. Solanki. They combine standard Zürich wine-glass modeling with “1.5D radiative transfer” (cf. Solanki et al. 1991) by computing annular 3D averages of emergent spectra along many rays that slant at viewing angle $\mu = 0.88$ through a 2D row of multiple flaring and merging rotationally symmetric fluxtubes, as illustrated in Fig. 5 of Bünte et al. (1993). The PLA model parameters correspond to magnetic surface filling factor 25% and a fluxtube merging height of 360 km.

Calibration to absolute intensity. The spectral intensities were calibrated to absolute intensities through the quiet-sun disk-center fit to the Brault-Neckel atlas obtained with the line-haze corrections and HSRA-SP-M modification described above. Spectral synthesis for $\mu = 0.88$ with these fitting parameters was found to correspond well with the Brault-Neckel atlas after scaling the latter to viewing angle $\mu = 0.88$ with the limb-darkening coefficients of Makarova et al. (1998). The observed spectrogram brightness scales were then converted into absolute units by scaling the mean spectrum averaged over subsets of quiet-sun pixels in the spectrograms to the synthetic spectra.

Dopplershift determination. The narrow blends that are superimposed on the H and K wings provide convenient Dopplershift samplers spanning a considerable height in their velocity response. We selected 23 Ca II K blends and 17 Ca II H blends with well-defined cores for Dopplershift measurement. They are identified in Fig. 4. The measurement follows Brandt et al. (1997) in defining the line core extent as the lower two-tenths of the profile and obtaining its displacement as the first moment of the line depression after interpolation to 1 mÅ sampling. The displacements are measured relative to a quiet-sun average estimated from less magnetic areas along the slit. Their scarcity implies a less good reference than might have been obtained from a quiet-sun area.

Detailed blend modeling was performed to put these measurements on a common height scale. For each blend the oscillator strength was varied to fit the observed line-center intensity in each bright-point spectrum with the corresponding bright-point model. Microturbulent broadening of 1.6 km s^{-1} was assumed at all heights. The contribution function to the line depression was then computed from each fit. Its first moment defines the representative sampling height.

4. Results

Bright-point models. Figure 5 shows the observed Ca II K wing spectra for the nine selected bright points marked in Fig. 1. The Ca II K core is doubly-peaked, in most cases with varying asymmetry. The inner and outer wings vary considerably between different bright points, as evident when compared with the quiet-sun spectrum which is the same in the different panels (as are the asterisks for PLA), but in all cases the bright-point profile lies well above the quiet-sun profile

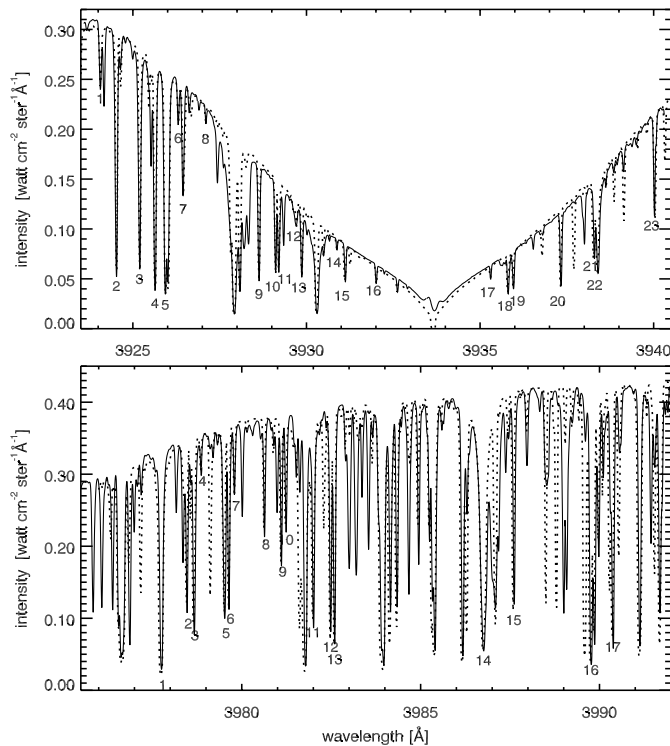


Fig. 4. Observed segments of the H and K lines. *Upper panel:* Ca II K. *Lower panel:* red wing of Ca II H. Solid: disk-center intensity spectra from the Brault-Neckel atlas. Dotted: synthesized from HSRA-SP-M. The numbered lines are used for Dopplershift determination.

throughout the Ca II K wings. There are no obvious systematic relationships between line core, inner wing, and outer wing behavior. Figure 6 shows the corresponding results for the five Ca II H pixels marked in Fig. 2. The bright-point spectra are again brighter than the quiet-sun reference spectrum in all cases at all wavelengths.

The asterisk symbols in Figs. 5 and 6 result from the PLA model using spatial wine-glass averaging. In the outer H and K wings this model produces higher intensities than all bright-point spectra, but the steeper slopes towards Ca II K line center make the inner wings drop below some bright-point spectra.

The plus symbols in Figs. 5 and 6 overlying the bright-point spectra mark our computed fits to the observed intensities at the wavelengths within blend-free wing windows that we selected for model fitting. They result from trial-and-error adjustment of the thin fluxtube model including recomputation of the hydrostatic densities, ionization equilibria, continuous and line opacities, and the magnetic field stratification.

The corresponding temperature stratifications are shown in Fig. 7, with the HSRA-SP-M and PLA models added for reference. The adjustment uncertainty per model is about 50 K. The height scale is common to all; it has $h = 0$ at $\tau_5 = 1$ for the outside HSRA-SP-M model. The superimposed symbols show the resulting fit values for three selected pixels, one for Ca II H and two for Ca II K, which span the spread between the different models. They lie at the computed brightness temperature at the corresponding formation height (defined as the first moment of the intensity contribution function) per fitting wavelength.

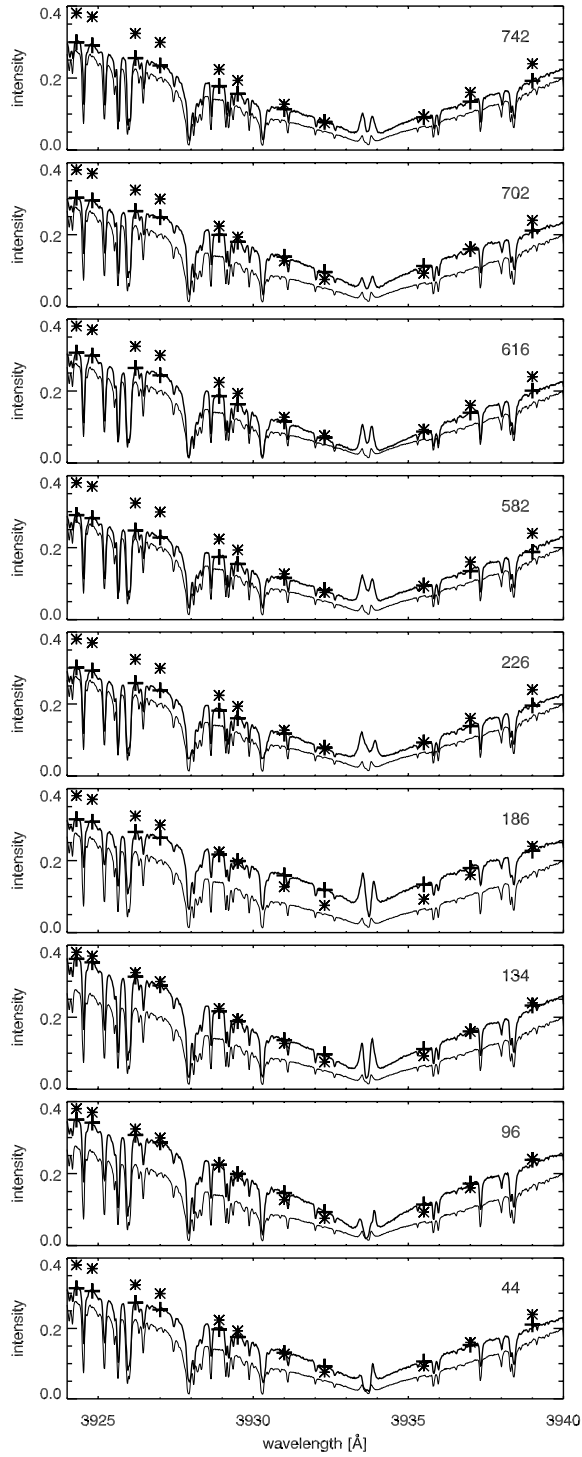


Fig. 5. Bright-point Ca II K spectra and model fits. The tracings are absolute intensities derived from the Ca II K spectrogram in Fig. 1, in units $\text{W m}^{-2} \text{ster}^{-1} \text{Å}^{-1}$. Thick upper curves: individual bright point spectra, identified by their pixel row number. Thin lower curves: quiet-sun average, repeated in each panel as reference. Plus symbols: absolute intensities from the best-fit model for each bright point. The corresponding temperature stratifications are shown in Fig. 7. Star symbols: absolute intensities computed from the PLA model with spatial “wine-glass” averaging, the same in each panel.

Their heights identify the range over which our trial-and-error adjustment defines each model most sensitively. The deepest

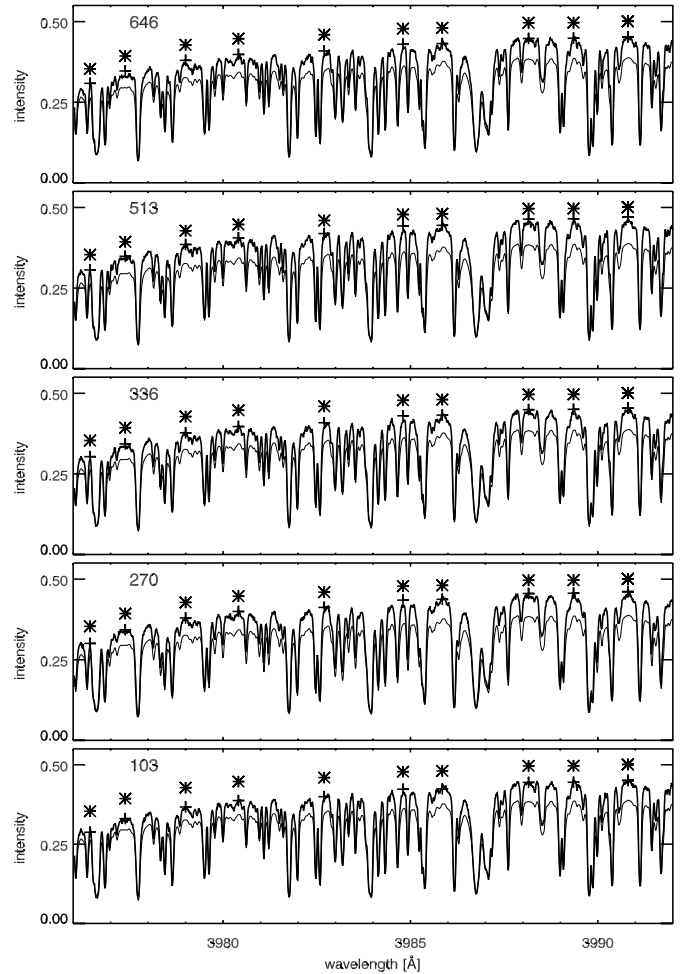


Fig. 6. Ca II H red-wing spectra and modeling in the format of Fig. 5.

layers are sampled best by the outer H-wing wavelengths, for which the bright-point models are on average slightly hotter than the Ca II K fits.

The fourteen best-fit models have similar shapes, with model-to-model differences of a few hundred Kelvin at any height. They all show a smooth outward temperature decline cutting through the hump in the PLA model. The lefthand panel of Fig. 7 shows that at equal geometrical height, up to $h \approx 200$ km, they are all much cooler than the outside model. Therefore, the bright-point intensity excesses observed at all wing-sampling wavelengths in Figs. 5 and 6 represent hotter gas only in the actual photon-escape regions, which lie much deeper within the fluxtubes than outside. This escape-depth difference, i.e. the fluxtube Wilson depression, is the main cause of the observed fluxtube brightening throughout the H and K wings. This is illustrated by the righthand panel of Fig. 7, which shows each model replotted on the continuum optical depth scale belonging to each individual model. In this plot the bright-point models decay less steeply with decreasing optical depth than the outside HSRA-SP-M, from rather similar values around $\tau_5 = 1$. The horizontal displacements from the HSRA-SP-M between same-wavelength symbols in the lefthand panel imply Wilson depressions of about 200 km. The slight $\log \tau_5$ shifts in characteristic formation locations

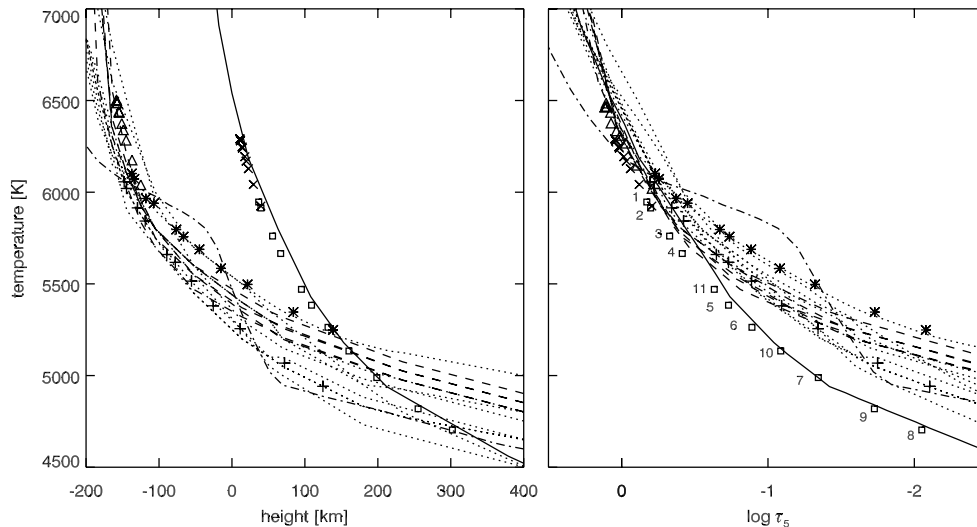


Fig. 7. Temperature stratifications of the best-fit bright-point models. The dotted curves correspond to the nine Ca II K fits in Fig. 5, the dashed curves to the five Ca II H fits in Fig. 6. *Left*: temperature against height, with a common height scale for all models. *Right*: temperature against the continuum optical depth at 5000 Å in each model. The symbols mark the computed brightness temperature at the corresponding formation height for the different fitting wavelengths: asterisks for Ca II K pixel row 186, pluses for Ca II K row 226, triangles for Ca II H row 270. The HSRA-SP-M (solid) and PLA (dot-dashed) models are added for comparison. The crosses and squares along HSRA-SP-M are Ca II H and Ca II K brightness temperatures, respectively, at the height of formation computed for $\mu = 0.88$ from this model at the fitting wavelengths. For Ca II K the latter are numbered in order of increasing wavelength (cf. Fig. 5) in the righthand panel. The crosses for the Ca II H fitting wavelengths (cf. Fig. 6) lie deeper for longer wavelength.

between the bright-point models and the HSRA-SP-M are caused by density sensitivity to temperature through the magnetostatic pressure constraint.

Dopplershifts. The displacement measurements for the blend cores marked in Fig. 4 are shown in Fig. 8. Blend numbers are added in two center-row panels to indicate which blend samples which height (small shifts occur between different bright points). The measured Dopplershifts range between -1 and $+1$ km s $^{-1}$, with smaller spread per bright point. Some bright points show slight but significant Dopplershift gradients with height. These results agree with the velocity measurements from Stokes profiles by Sigwarth et al. (1999) for the larger-size magnetic elements in their data and the more recent measurements from adaptive-optics Dopplergrams by Rimmele (2004).

5. Discussion

Comparison with RE modeling. In Fig. 9 we compare our best-fit bright point models with standard plane-parallel radiative-equilibrium (RE) modeling. The thick curves are averages over the nine Ca II K and five Ca II H fits, respectively. The deepest layers are best constrained by the H-wing models, the higher layers are by the K-wing models (Fig. 7). The HSRA-SP-M (solid) and PLA (dot-dashed) models are added for comparison. Two RE models are shown, for $T_{\text{eff}} = 6200$ K (thin dashed) and $T_{\text{eff}} = 5777$ K (dotted), respectively, with solar values for the other parameters ($\log g = 4.44$, solar abundances). They were kindly computed by Ya. V. Pavlenko using his modification (Pavlenko 2003) of the ATLAS12 code

of Kurucz (1993, 1996). Comparison of HSRA-SP-M and RE-5777 confirms that the former is close to RE above $\log \tau_5 \approx 0$, confirming the well-known property of the solar photosphere to by-and-large obey radiative equilibrium as established originally by Schwarzschild (1906; translation in Menzel 1966). The RE-6200 model, of which the effective temperature is selected to mimic the HSRA-SP-M reproduction for the bright-point averages, duplicates the K-fit mean above $\log \tau_5 \approx -0.4$. This suggests that also fluxtube photospheres approximately obey radiative equilibrium, i.e. that the shallower outward decay of the bright-point models with respect to the outside atmosphere does not imply non-radiative heating.

The bright point spectra in Figs. 5 and 6 are all more intense than the quiet-sun spectrum at all wavelengths. The static radiative cooling budget in Fig. 49 of Vernazza et al. (1981) and its elaboration by Avrett (1985) identify the H and K lines as strong non-RE coolers in the low chromosphere. They also act as dominant radiation losers in the dynamic modeling of Carlsson & Stein (1997). Thus, enhanced emission in the H and K line centers is direct evidence of chromospheric heating. In contrast, our bright-point stratifications are much cooler than the outside atmosphere and not heated significantly above radiative-equilibrium values. The enhanced brightness of the H and K wings in Figs. 5 and 6 derives primarily from the large Wilson depression that results from magnetic-element evacuation. The non-radiative heating which causes the K₂ emission peaks in Fig. 5 sets in only at larger height. We conclude that mechanical heating within magnetic elements becomes important only above $h \approx 200$ km. This holds also for whatever constitutes the basal H and K surface flux from cool stars (Rutten et al. 1991; Schrijver 1995).

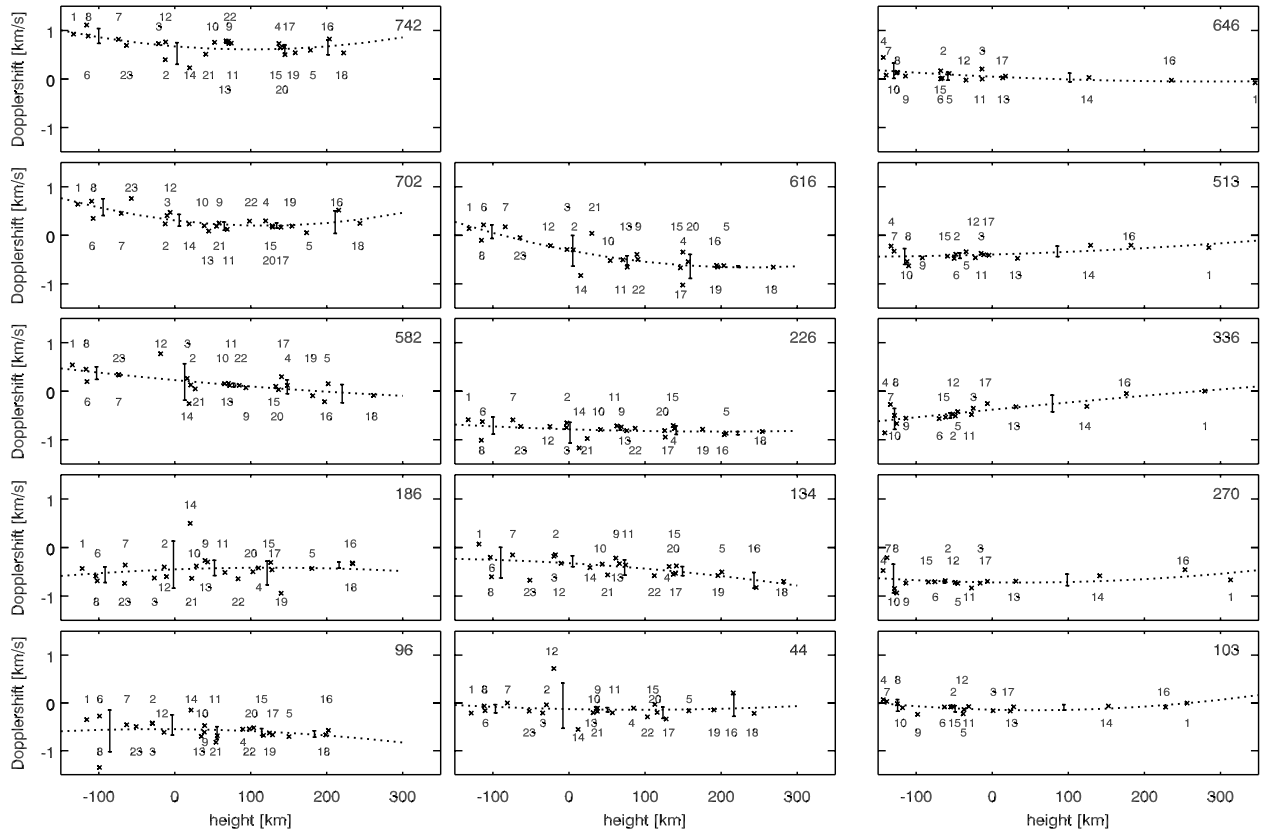


Fig. 8. Dopplershifts against height. Positive values imply downdrafts. For purely vertical motions the actual speeds are 14% larger due to the $\mu = 0.88$ viewing projection. First two columns: measured from Ca II K blends. Third column: measured from Ca II H blends. The pixel row numbers are specified per panel. The numbers identify the blends as in Fig. 4. The dotted curves are polynomial fits. The error bars show the rms spread per five-point bin.

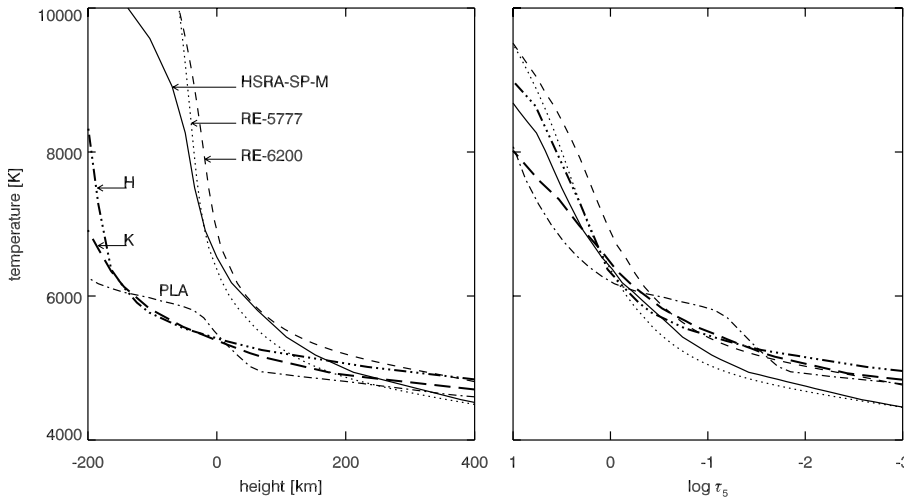


Fig. 9. Comparison between bright point models and RE modeling. *Left:* against height. *Right:* against continuum optical depth at 5000 Å in each model. Thick curves: averages of the nine Ca II K (long dashes) and the five Ca II H (dash-triple dot) bright point models, respectively. Thin dashed curve: RE model for $T_{\text{eff}} = 6200$ K. Dotted: standard solar RE model for $T_{\text{eff}} = 5777$ K. The HSRA-SP-M (solid) and PLA (dash-dot) models are again added for comparison.

Below the surface the bright-point averages have shallower temperature gradients than for RE modeling, as it is the case for the outside HSRA-SP-M model as modified by Spruit (1974) to admit convection and for the theoretical thin-tube models of Hasan & Kalkofen (1994) which also include convective energy transport.

Comparison with the PLA model. The asterisks in Figs. 5 and 6 show that the PLA model combined with Zürich

wine-glass averaging predicts too steep inward temperature increase in all cases, although the model is not significantly hotter than our best fits. The higher brightnesses arise because in annular wine-glass averaging the outside atmosphere gains larger weight at increasing wavelength separation from line center due to increasing canopy transparency. Unpublished wine-glass modeling by D. B. Roy of the outer Ca II H wing in Fig. 2 showed that with PLA geometry it is virtually defined by the outside rather than the inside model, as sampled by off-axis

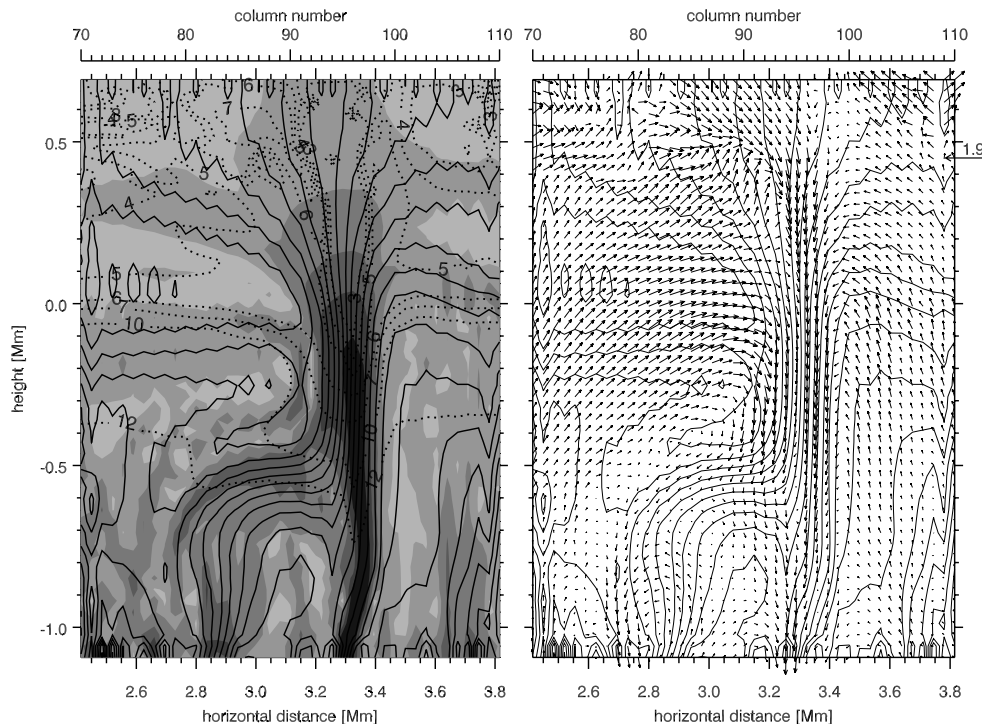


Fig. 10. Segment of a snapshot from a numerical magnetoconvection simulation by Gadun (2000), selected because it contains a strong near-vertical magnetic field concentration reminiscent of an idealized fluxtube. It is located at $t = 116.5$ min in the complete timeslice shown in Fig. 1 of Gadun et al. (2001). The column width is 35 km, corresponding to 0.05 arcsec. The vertical height scale has $h = 0$ km at $\tau_5 = 1$ along Col. 74. *First panel:* lighter greyscale shades correspond to field strengths above 2000, 1500, 1000, 500, 200, and 10 Gauss, respectively. Solid curves: magnetic field lines. Dotted curves: isotherms labeled with their temperature value in units of 1000 K. *Second panel:* velocity field. One flow arrow is marked with the corresponding speed in km s^{-1} .

rays cutting through the flaring tube flanks. We have similarly tried to fit our inner-wing Ca II K spectra with wine-glass PLA modeling but found that their reproduction requires either large case-by-case adjustment of the quiet-sun outside atmosphere or exceedingly large adjustments of the inside stratification with very large variations between different bright points. The imposed flaring makes the inside contribution too small. We suspect that the PLA wine-glass geometry overestimates the actual fluxtube spreading considerably. At our high angular resolution one-dimensional on-axis modeling becomes a better approach.

The individual bright point models in Fig. 7 cut smoothly through the hump in the PLA model. Their average in Fig. 9 does the same and follows the RE-6200 model closely in the PLA hump region. The marked difference between the PLA hump and RE behavior was noted by Stuik et al. (1997) in the context of cool-star activity modeling and discussed by Rutten et al. (2001) in the context of G-band contrast enhancement. The righthand panel of Fig. 9 shows that the hump is centered at optical depth $\log \tau_5 = -1$ where the Ca II K model fits are best defined and display RE behavior. The PLA hump implies additional heating at this location combined with abrupt cooling causing the steep decline higher up. We interpret it rather as an artifact from the assumption of LTE opacities for the Fe I lines used in the PLA Stokes profile fitting. In particular, we suspect that near-ultraviolet hot-wall radiation ionizes iron (and other minority atoms) to higher degree than expected

from 1D modeling even when the latter includes NLTE ionization as in Solanki & Steenbock (1988). Larger actual ionization produces opacity reduction and line weakening. The latter is modeled as source function excess in Stokes profile fits, hence as too high temperature. Neglect of sideways overionization similarly affects the Stokes-profile modeling of Hasan et al. (1998) and the Stokes-profile inversions of Bellot Rubio et al. (2000). Note that also Fe II lines are prone to NLTE weakening, not from opacity deficits but from overexcitation due to ultraviolet pumping (Cram et al. 1980; cf. Rutten 1988).

Comparison with numerical simulation. Figure 10 shows a snapshot from a two-dimensional magnetoconvection simulation by the late A. S. Gadun. It was described in Gadun (2000) and also employed in Gadun et al. (2001). The snapshot is a cutout part of the vertical simulation plane at a selected location and time where a well-developed, sizable magnetic element exists which resembles an idealized magnetic fluxtube in its field strength and in being fairly straight and vertical. The greyscale coding in the first panel represents magnetic field strength, the solid curves are magnetic field lines, the dotted curves isotherms. The diameter of the magnetic element varies from 50 km to 200 km depending on contour choice. The second panel shows the flow field at the same instant.

The temperature, magnetic field and vertical velocity stratifications of this simulated fluxtube are compared to our

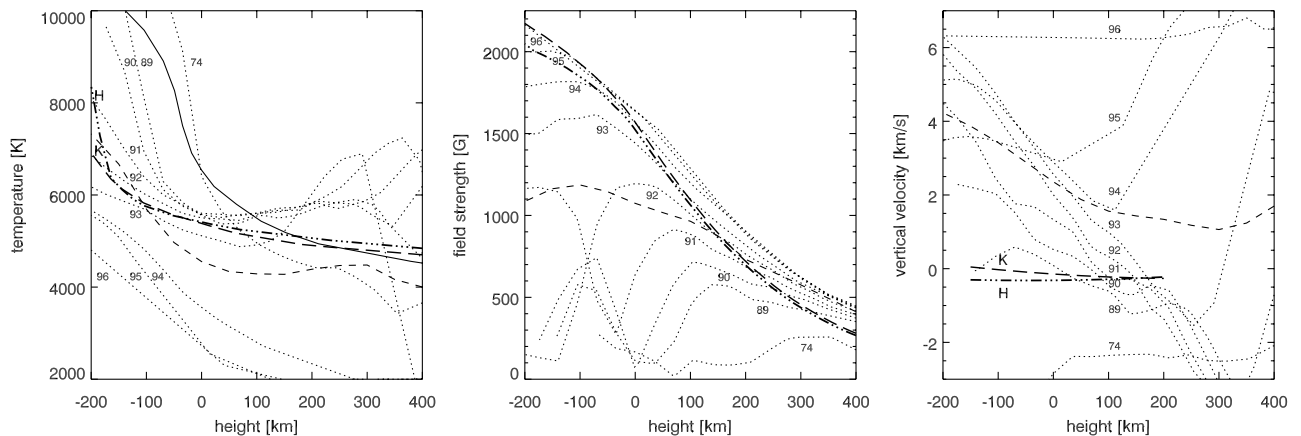


Fig. 11. Comparison between the empirical bright point models and the numerical simulation. Dotted curves: values along simulation snapshot Cols. 89–96 of Fig. 10. Thin dashed curves: average over these fluxtube columns. Thick curves: averages of the nine Ca II K (long dashes) and five Ca II H (dash-triple dot) bright point models. *First panel:* temperature stratifications. The solid curve is the HSRA-SP-M model. *Second panel:* magnetic field strengths. *Third panel:* vertical velocities in the simulation and measured Dopplershifts.

bright-point fits in Fig. 11. In each panel the dotted curves are the simulation stratifications along the adjacent Cols. 89–96, marked by their column number as specified along the top of Fig. 10. The thin dashed curve in each panel is the spatial average over these magnetic-element columns. The dotted curves for Col. 74 represent a location without much magnetic field as representing quiet sun. It samples a granule interior and thus shows an upflow in the third panel of Fig. 11. It is hotter than HSRA-SP-M (solid) below the surface while cooler higher up, as expected since HSRA-SP-M represents a spatial average over the granulation and its reversal in higher layers. The averages over the 9 best-fit Ca II K and 5 best-fit Ca II H bright point models are again added in each panel. The best-fit magnetic field stratifications in the second panel are constrained by the imposed base value and requiring magnetostatic equilibrium at all heights.

The correspondence with the the simulation fluxtube stratifications is reasonable with respect to temperature and field strength over the -200 to $+200$ km height range sampled by the H and K wings. However, the simulation fluxtube contains a strong downdraft, particularly along its axis (Col. 96), whereas the Dopplershifts from the bright point spectra average to nearly zero. Statistics for the complete simulation ($3880 \text{ km} \times 2 \text{ h}$) were reported in Sheminova (2004). The strong-field elements generally contain downdrafts, on average about 3 km s^{-1} but up to 9 km s^{-1} in extreme cases. Areas with weak diffuse field tend to contain weak upflows, up to 3 km s^{-1} with 0.5 km s^{-1} on average. The magnetic element selected here belongs to the more extreme downdraft class. Comparable simulations by Grossmann-Doerth et al. (1998) predict large downdrafts during the magnetic-element formation stage but smaller ones for more stable fluxtubes, and suggest that the latter are mostly due to entrainment by adjacent downdrafts (Steiner et al. 1998).

Incomplete resolution. Our bright points appear as fairly isolated entities in the Ca II K slitjaw image in Fig. 1 and may resemble the isolated simulated magnetic element in Fig. 10,

but undoubtedly they are not fully resolved in the spectrograms and the latter certainly fail to resolve horizontal gradients as large as in Fig. 10. In addition, actual magnetic elements are likely to often possess tilts. Nevertheless, the much better consistency between the fourteen fits in Fig. 7 than we obtained initially from PLA-model wine-glass averaging suggests that 1D H and K wing modeling is a fair approach at the angular resolution reached here.

Note that the classical flaring-fluxtube geometry with extended canopies merging at chromospheric heights is called “fundamentally wrong” by Schrijver & Title (2003) on the premise that much network field loops back down already over short horizontal distance. In contrast, Rimmele (2004) detects slower-than-PLA wine-glass spreading. Note also that a particularly sharp G-band image from the SST discussed recently by Berger et al. (2004) reveals magnetic elements of more complex “ribbon” and “flower” morphology than tube-like bright points. In contrast, Wiehr et al. (2004) measure G-band bright points as mostly being roundish and resolved by the SST.

Our 1D modeling describes in principle the stratification of vertical magnetic elements along their axes. In practice, hot-wall radiation is bound to enhance the apparent brightness along lines of sight cutting through the walls. The actual temperatures in magnetic-element cores may therefore be even cooler than in our fits. The slight temperature excess of the H-wing fits over the K-core fits in the region of overlap (first panel of Fig. 7) may result from the lower angular resolution of the H-wing spectrogram.

With incomplete resolution our result that radiative equilibrium seems to apply may hold for transverse spatial averages over horizontal photon-diffusion length scales. Magnetic elements are then to be interpreted as deep dips in the photon-escape surface of a highly warped atmosphere which is in or close to radiative equilibrium above the convective regime in a spatially-averaged sense.

Incomplete resolution affects our Dopplershift determination most where large horizontal gradients occur. This is the case across the example fluxtube in Fig. 10, of which our

near-0.2 arcsec resolution would smear at least four columns. Large gradients may also result from strong narrow down-drafts bordering magnetic elements, as suggested by Stokes polarimetry and simulations (e.g. van Ballegoijen 1985; Grossmann-Doerth et al. 1988; Leka & Steiner 2001).

The utter limit of incomplete resolution is represented by 1D “standard model” fitting of spatially-averaged disk-center spectra as exemplified in Fig. 3. The classical notion that spatially-averaged spectra can be described satisfactorily by a single 1D model is perhaps reasonable in the upper internetwork photosphere where reversed granulation (Rutten et al. 2004) and acoustic oscillations (Krijger et al. 2001) constitute most of the observed fine structure as modulations with relatively small amplitudes. Over $h \approx 200\text{--}400$ km we deem our HSRA-SP-M fit of the H and K wings, which recovers the FALC continuum model, more reliable than the 1D models based on LTE fits of FeI and FeII lines used traditionally in abundance determination. However, the notion fails increasingly at larger depth where convection reigns. There, single-pixel spectrometry must replace unresolved spectrometry just as 3D simulation has replaced 1D modeling.

6. Conclusion

The extended wings of Ca II H and K provide relatively straightforward diagnostics of the temperature and line-of-sight velocity stratifications in the solar photosphere. We have used them to diagnose individual magnetic elements in plage. Our fits to high-resolution H and K spectra of fourteen bright points correspond well with earlier plage modeling based on low-resolution Stokes profile fitting. The bright points are brighter than their surroundings throughout the H and K wings, but their temperature stratifications are appreciably cooler than the quiet sun outside and are close to radiative equilibrium throughout their photosphere. A fluxtube-like magnetic concentration in Gadun’s 2D magnetoconvection simulation shows similar temperature and field stratifications but the measured Dopplershifts are much smaller than the large downdraft in the simulated tube.

Our spectrograms were obtained with the SVST of 48 cm aperture. It has been replaced by the 1-m SST which employs adaptive optics and was recently equipped with a spectrometer. Wavefront-restored spectrometry with this telescope and with future other meter-class solar telescopes brings substantially higher angular resolution than reached here. Resolved-feature analysis using the Ca II H and K wings will be a fruitful approach to analyze small-scale structures and their dynamics throughout the solar photosphere. Extension of our modeling to large-volume data inversion is relatively easy thanks to the LTE behavior of both the H and K wing opacities and source functions. For the same reasons the H and K wings are also relatively easy synthesized from numerical simulations, as recently done by Leenaarts & Wedemeyer-Böhm (2005) for a 3D granulation simulation. We look forward to resolved-structure analysis of photospheric fine structure using the H and K wings as a regular tool in solar high-resolution observations and MHD simulations.

Acknowledgements. We are grateful to the observing staff of the SVST for much assistance, to Sami Solanki for sharing his fluxtube geometry codes, to Jakiv Pavlenko for computing the RE models, to Luis Bellot Rubio for advice on magnetostatic thin-tube modeling, and to Daniel Roy for insights from PLA-like modeling. Referee S. Wedemeyer-Böhm suggested many improvements to the paper. The SVST was part of the Spanish Observatorio del Roque de los Muchachos of the Instituto de Astrofísica de Canarias and operated by the Royal Swedish Academy of Sciences. Our Utrecht-Oslo collaboration is part of the European Solar Magnetism Network supported by the European Commission under contract HPRN-CT-2002-00313, which also funds L. H. M. Ruppe van der Voort. Our Kiev-Utrecht collaboration is supported by INTAS under contract 00-00084. V. A. Sheminova acknowledges hospitality at Deil and Utrecht. R. J. Rutten acknowledges travel support from the Leids Kerkhoven-Bosscha Fonds and hospitality at Kiev. This research has made much use of NASA’s Astrophysics Data System.

References

- Avrett, E. H. 1985, in *Chromospheric Diagnostics and Modeling*, ed. B. W. Lites, NSO/SP Summer Conference, Sunspot, 67
- Ayres, T. R. 1975, *ApJ*, 201, 799
- Ayres, T. R. 1977, *ApJ*, 213, 296
- Ayres, T. R. 1989, *Sol. Phys.*, 124, 15
- Ayres, T. R., & Linsky, J. L. 1975, *ApJ*, 200, 660
- Ayres, T. R., Linsky, J. L., & Shine, R. A. 1974, *ApJ*, 192, 93
- Barklem, P. S., & O’Mara, B. J. 1998, *MNRAS*, 300, 863
- Beckers, J. M., & Schröter, E. H. 1968, *Sol. Phys.*, 4, 142
- Bellot Rubio, L. R., & Borrero, J. M. 2002, *A&A*, 391, 331
- Bellot Rubio, L. R., Ruiz Cobo, B., & Collados, M. 1996, *A&A*, 306, 960
- Bellot Rubio, L. R., Ruiz Cobo, B., & Collados, M. 2000, *ApJ*, 535, 489
- Berger, T. E., Ruppe van der Voort, L. H. M., Löfdahl, M. G., et al. 2004, *A&A*, 428, 613
- Brandt, P. N., Gadun, A. S., & Sheminova, V. A. 1997, *Kinematika i Fizika Nebesnykh Tel.*, 13, 65
- Brault, J. W. 1978, in *Future solar optical observations: needs and constraints*, ed. G. Godoli, G. Noci, & A. Righini, Proc. JOSO Workshop (Florence: Osservazioni e Memorie Oss. Astrof. Arcetri), 33
- Brault, J. W. 1993, in *Selected Papers on Instrumentation in Astronomy*, ed. W. Livingston, & B. J. Thompson, SPIE Milestone Series, 87, 273
- Briand, C., & Solanki, S. K. 1995, *A&A*, 299, 596
- Bruls, J. H. M. J., & Solanki, S. K. 1993, *A&A*, 273, 293
- Bruls, J. H. M. J., Rutten, R. J., & Shchukina, N. G. 1992, *A&A*, 265, 237
- Büntje, M., Solanki, S. K., & Steiner, O. 1993, *A&A*, 268, 736
- Carlsson, M., & Stein, R. F. 1997, *ApJ*, 481, 500
- Carlsson, M., Stein, R. F., Nordlund, Å., & Scharmer, G. B. 2004, *ApJ*, 610, L137
- Cram, L. E., Rutten, R. J., & Lites, B. W. 1980, *ApJ*, 241, 374
- Defouw, R. J. 1976, *ApJ*, 209, 266
- Dunn, R. B., & Zirker, J. B. 1973, *Sol. Phys.*, 33, 281
- Fontenla, J. M., Avrett, E. H., & Loeser, R. 1993, *ApJ*, 406, 319
- Frazier, E. N., & Stenflo, J. O. 1972, *Sol. Phys.*, 27, 330
- Gadun, A. S. 2000, *Kinematika i Fizika Nebesnykh Tel.*, 16, 99
- Gadun, A. S., & Sheminova, V. A. 1988, SPANSAT: Program for calculating absorption line profiles in stellar atmospheres in LTE approximation, Inst. Theor. Physics Ukrainian Acad. Sciences, preprint No. ITF-88-87P

- Gadun, A. S., Solanki, S. K., Sheminova, V. A., & Ploner, S. R. O. 2001, *Sol. Phys.*, 203, 1
- Gingerich, O., Noyes, R. W., Kalkofen, W., & Cuny, Y. 1971, *Sol. Phys.*, 18, 347
- Grevesse, N., & Sauval, A. J. 1999, *A&A*, 347, 348
- Grossmann-Doerth, U., Schüssler, M., & Solanki, S. K. 1988, *A&A*, 206, L37
- Grossmann-Doerth, U., Knölker, M., Schüssler, M., & Solanki, S. K. 1994, *A&A*, 285, 648
- Grossmann-Doerth, U., Schüssler, M., & Steiner, O. 1998, *A&A*, 337, 928
- Hasan, S. S., & Kalkofen, W. 1994, *ApJ*, 436, 355
- Hasan, S. S., Kneer, F., & Kalkofen, W. 1998, *A&A*, 332, 1064
- Holweger, H., & Müller, E. A. 1974, *Sol. Phys.*, 39, 19
- Howard, R., & Stenflo, J. O. 1972, *Sol. Phys.*, 22, 402
- Keller, C. U., Steiner, O., Stenflo, J. O., & Solanki, S. K. 1990, *A&A*, 233, 583
- Keller, C. U., Schüssler, M., Vögler, A., & Zakharov, V. 2004, *ApJ*, 607, L59
- Knölker, M., & Schüssler, M. 1988, *A&A*, 202, 275
- Krijger, J. M., Rutten, R. J., Lites, B. W., et al. 2001, *A&A*, 379, 1052
- Kupka, F., Piskunov, N., Ryabchikova, T. A., Stempels, H. C., & Weiss, W. W. 1999, *A&AS*, 138, 119
- Kurucz, R. L. 1993, in *Peculiar versus Normal Phenomena in A-type and Related Stars*, IAU Coll., 138, ASP Conf. Ser., 44, 87
- Kurucz, R. L. 1996, in *M.A.S.S., Model Atmospheres and Spectrum Synthesis*, ASP Conf. Ser., 108, 160
- Labs, D., & Neckel, H. 1972, *Sol. Phys.*, 22, 64
- Leenaarts, J., & Wedemeyer-Böhm, S. 2005, *A&A*, 431, 687
- Leka, K. D., & Steiner, O. 2001, *ApJ*, 552, 354
- Livingston, W., & Harvey, J. 1969, *Sol. Phys.*, 10, 294
- Makarova, E. A., Kharitonov, A. V., Kaznachevskaja, T. V., Roshchina, E. M., & Sarychev, A. P. 1998, *Baltic Astronomy*, 7, 467
- Menzel, D. H. 1966, *Selected Papers on the Transfer of Radiation* (New York: Dover Pub.)
- Muller, R. 1983, *Sol. Phys.*, 85, 113
- Muller, R., & Roudier, T. 1984, *Sol. Phys.*, 94, 33
- Neckel, H. 1999, *Sol. Phys.*, 184, 421
- Neckel, H., & Labs, D. 1984, *Sol. Phys.*, 90, 205
- Pavlenko, Y. V. 2003, *Astronomy Reports*, 47, 59
- Priest, E. R., & Forbes, T. G. 2001, in *Encyclopedia of Astronomy and Astrophysics*, ed. P. Murdin (Bristol: Institute of Physics Publishing), 1540
- Rimmele, T. R. 2004, *ApJ*, 604, 906
- Roberts, B., & Webb, A. R. 1978, *Sol. Phys.*, 56, 5
- Roupe van der Voort, L. H. M. 2002a, *A&A*, 389, 1020
- Roupe van der Voort, L. H. M. 2002b, *Sunspot structure and dynamics* (Stockholm University: Ph.D. Thesis)
- Rutten, R. J. 1988, in *Physics of Formation of FeII Lines Outside LTE*, ed. R. Viotti, A. Vittone, & M. Friedjung (Dordrecht: Reidel), IAU Coll., 94, 185
- Rutten, R. J. 2002, *J. Astron. Data*, 8, 8
- Rutten, R. J., & Kostik, R. I. 1982, *A&A*, 115, 104
- Rutten, R. J., & Uitenbroek, H. 1991, *Sol. Phys.*, 134, 15
- Rutten, R. G. M., Schrijver, C. J., Lemmens, A. F. P., & Zwaan, C. 1991, *A&A*, 252, 203
- Rutten, R. J., Kiselman, D., Roupe van der Voort, L., & Plez, B. 2001, in *Advanced Solar Polarimetry – Theory, Observation, and Instrumentation*, ed. M. Sigwarth, *Procs. 20th NSO/SP Summer Workshop*, ASP Conf. Ser., 236, 445
- Rutten, R. J., de Wijn, A. G., & Stütterlin, P. 2004, *A&A*, 416, 333
- Scharmer, G., Brown, D., Petterson, L., & Rehn, J. 1985, *Appl. Opt.*, 24, 2558
- Schrijver, C. 1995, *A&AR*, 6, 181
- Schrijver, C. J., & Title, A. M. 2003, *ApJ*, 597, L165
- Schwarzschild, K. 1906, *Nachrichten Königlichen Gesellschaft Wissensch. Göttingen. Math.-Phys. Klasse*, 195, 41
- Sheeley, N. R. 1967, *Sol. Phys.*, 1, 171
- Sheminova, V. A. 2004, *Kinematika i Fizika Nebesnykh Tel.*, 20, 3
- Shine, R. A., & Linsky, J. L. 1974, *Sol. Phys.*, 37, 145
- Shine, R. A., Milkey, R. W., & Mihalas, D. 1975, *ApJ*, 199, 724
- Sigwarth, M., Balasubramaniam, K. S., Knölker, M., & Schmidt, W. 1999, *A&A*, 349, 941
- Solanki, S., Steiner, O., & Uitenbroek, H. 1991, *A&A*, 250, 220
- Solanki, S. K. 1986, *A&A*, 168, 311
- Solanki, S. K., & Brigljevic, V. 1992, *A&A*, 262, L29
- Solanki, S. K., & Steenbock, W. 1988, *A&A*, 189, 243
- Solanki, S. K., & Steiner, O. 1990, *A&A*, 234, 519
- Solanki, S. K., Steiner, O., & Uitenbroek, H. 1991, *A&A*, 250, 220
- Spruit, H. C. 1974, *Sol. Phys.*, 34, 277
- Spruit, H. C. 1976, *Sol. Phys.*, 50, 269
- Spruit, H. C. 1977, *Magnetic flux tubes and transport of heat in the convection zone of the Sun*, Utrecht University: Ph.D. Thesis
- Spruit, H. C., & Zwaan, C. 1981, *Sol. Phys.*, 70, 207
- Steiner, O. 2005, *A&A*, 430, 691
- Steiner, O., Grossmann-Doerth, U., Knölker, M., & Schüssler, M. 1998, *ApJ*, 495, 468
- Stuik, R., Bruls, J. H. M. J., & Rutten, R. J. 1997, *A&A*, 322, 911
- Uitenbroek, H. 1989, *A&A*, 213, 360
- van Ballegooijen, A. A. 1985, in *Theoretical Problems in High Resolution Solar Physics*, ed. H. U. Schmidt, *Proc. Solar Opt. Tel. Workshop* (München: Max Planck Inst. Astrophysik), 177
- Vernazza, J. E., Avrett, E. H., & Loeser, R. 1981, *ApJS*, 45, 635
- Wiehr, E., Bovelet, B., & Hertzberger, J. 2004, *A&A*, 422, L63